Investigations on the Vorticity Sheets of a Close-Coupled Delta-Canard Configuration

Hans-Christoph Oelker* and Dietrich Hummel†
Technische Universität Braunschweig, Braunschweig, Federal Republic of Germany

Comprehensive aerodynamic investigations have been carried out on a close-coupled, $A = 2.31$ delta-canard configuration at low speed. Results of three-component, surface-pressure, and flowfield measurements, as well as oil-flow patterns, are presented for the canard-off and canard-on configurations. The main interference effects take place above the wing; the formation of the wing vortices is delayed considerably to positions downstream of the apex. The canard vortices pass the wing leading edge relatively high, and they are moved downward and inward above the wing. During this process, a fusion between the canard's vorticity sheet and the suction-side boundary layer of the wing takes place in the inner portion of the wing. The canard vortex system is maintained up to stations downstream of the wing trailing edge.

Nomenclature

Geometric Quantities

A = aspect ratio of canard or wing, $= b^2/S$
b = span of canard of wing, $= 2s$
$c(y)$ = local chord of canard or wing
c_r = root chord of canard or wing, $= c(y = 0)$
$\bar{c}$ = mean aerodynamic chord of the wing, $= 1/S_w \int_{-s_W}^{+s_W} c_W^2 \, dy_W$
e = distance between fuselage apex and wing geometric neutral point
H = dimensionless vertical position of the canard, $= \bar{h}/c_{rW}$
h = height of the fuselage
$\bar{h}$ = distance of the canard geometric neutral point N_{25C} from the fuselage axis
l_F = length of the fuselage
l_{1F}, l_{2F}, l_{3F} = length of front, cylindrical, and rear part of the fuselage
N_{25} = geometric neutral point of canard or wing
R = dimensionless relative forward position of the canard, $= (\bar{r} - \bar{r}_0)/c_{rW}$
$\bar{r}$ = horizontal distance between the geometric neutral points of canard and wing
$\bar{r}_0$ = horizontal distance between the geometric neutral points of canard and wing for canard trailing edge located at wing apex, $= (c_{rW} + c_{rC})/2$
S = area of canard or wing (extended to $Y_C = Y_W = 0$; see Fig. 1)
s = half span of canard or wing
$s_1(x)$ = local half span of canard or wing
t = maximum thickness of canard or wing or fuselage
x_{N25} = distance of geometric neutral point from origin of coordinate system for wing or canard, $= c_r/2$
x, y, z = body-fixed coordinates, origin at canard or wing apex
ϵ = setting angle of the canard; angle between the planes of canard and wing
$\bar{\zeta}_C$ = dimensionless aerodynamic coordinate with the origin at $x_W = y_W = z_W = 0$, $z_W \cdot \cos\alpha / s_C$
$\bar{\zeta}_W$ = dimensionless aerodynamic coordinate with the origin at the intersection of the measuring plane and the x_W-axis, $= z_W \cdot \cos\alpha / s_{1W}$
η = dimensionless local spanwise coordinate for canard or wing, $= y/s_1$
$\bar{\eta}_C$ = dimensionless aerodynamic coordinate with the origin at $x_W = y_W = z_W = 0$, $= y_W/s_C$
$\tilde{\eta}_W$ = dimensionless aerodynamic coordinate with the origin at the intersection of the measuring plane and the x_W axis, $= y_W/s_{1W}$
$\bar{\eta}_W$ = dimensionless aerodynamic coordinates with the origin at the intersection of the measuring plane with an axis parallel to the freestream, which passes through the point $x_W = c_{rW}$, $y_W = 0$, $z_W = 0$ at the trailing edge of the wing, $= y_W/s_W$
ξ = dimensionless body-fixed coordinate for canard or wing, $= x/c_r$
ϕ = leading-edge sweep of canard or wing

Aerodynamic Quantities

c_D = drag coefficient, $= D/q_\infty S_W$
c_g = total pressure coefficient, $= (g - p_\infty)/q_\infty$
c_L = lift coefficient, $= L/q_\infty S_W$,
c_m = pitching moment coefficient (reference point N_{25W}, nose-up positive), $= M/q_\infty S_W \bar{c}$
c_p = static pressure coefficient, $= (p - p_\infty)/q_\infty$
c_q = dynamic pressure coefficient, $= q/q_\infty$
g, p, q = total, static, and dynamic pressure respectively
q_∞ = freestream dynamic pressure
Re = Reynolds number, $= V_\infty \cdot c_{rW}/\nu$
V_∞ = freestream velocity
α = angle of attack; angle between freestream and wing plane, $z_W = 0$
ν = kinematic viscosity

Subscripts

C = canard
F = fuselage
W = wing

Introduction

A CLOSE-COUPLED canard configuration is a characteristic feature of modern fighter aircraft (e.g., Israel Aircraft Industries Lavi, SAAB Gripen, or European Fighter Aircraft). The physics of the corresponding three-dimensional and separated flow is, therefore, of high interest for aeronautical research work. Canard configurations have been investi-

Presented as Paper 88-5.4.1 at the 16th International Congress of the Astronautical Sciences, Jerusalem, Israel, Aug. 28–Sept. 2, 1988; received Oct. 29, 1988; revision received Jan. 28, 1989.

*Dipl.-Ing., Research Scientist, Institut für Strömungsmechanik.
†Prof. Dr.-Ing., Institut für Strömungsmechanik.

gated for a long time, and there exists a large number of published experimental works on this topic; however, these papers are mainly aimed at finding practicable configurations of aircraft design. Publications dealing with the physics of the flowfield and the interfering vortex systems from canard and wing are rare. Systematic investigations and detailed flowfield measurements were missing until now. In order to fill this gap, an extensive research program on close-coupled canard configurations was initiated at the Institut für Strömungsmechanik of the Technische Universität Braunschweig. The aim is to get detailed insight into the interference between the vortex systems of canard and wing and to provide experimental data for a comparison with theoretical results. In particular, it is intended to give a detailed quantitative documentation of the three-dimensional flowfield as was done earlier for the delta wing and double-delta wings.

It has been known since Behrbohm[1] that close-coupled canard configurations with canard and wing of small aspect ratios in the range of $1 \leq A \leq 3$ have substantial advantages. The value of maximum-lift coefficient $c_{L\max}$ and the corresponding angle of attack $\alpha(c_{L\max})$ can be increased considerably by adding a delta canard to a delta wing. This advantage is due to favorable interference between the vortex systems of canard and wing.[1]

Besides Behrbohm,[1] there are many papers on canard configurations. An early series of experiments was carried out at NASA in the 1950's[2-8] in which long-coupled canard configurations were tested. Later, a second series of measurements was performed at the Naval Ship Research and Development Center[9-12] and a third series at NASA.[13-20] These last two series were concerned with close-coupled canard configurations and were aimed at finding practicable configurations. Other work by Eberle et al.[21] and Goldstein and Combs[22] deal with trimming capabilities of close-coupled canard configurations in comparison with conventional configurations. John and Kraus[23] and Kraus[24] also investigated the aerodynamics of close-coupled canard configurations beyond stall. Investigations on the physics of the interfering vortex systems of canard and wing were performed by Gloss and Miner,[25] Lorincz,[26] and Er-El and Seginer,[27] but these papers give mainly qualitative insight into the flow structure by flow visualization. Quantitative work was done by Gallington and Sisson,[28] Griffin,[29] Griffin et al.,[30] Griffin and Jonas,[31] and Hjelmberg.[32] References 26 and 29-31 deal with canard configurations that have a forward-swept wing. The results of Refs. 28-31 are flowfield measurements in symmetrical and incompressible flow. The development of vorticity sheets is not presented. Reference 32 contains results that were obtained with the two European models of the International Vortex Flow Experiment on Euler Code Validation in symmetrical and compressible flow. These results also do not show the development of vorticity sheets.

Investigations performed at the Institut für Strömungsmechanik of Technische Universität Braunschweig are concerned with two different configurations. Figure 1 shows the sharp-edged delta wing configuration with $A_C = A_W = 2.31$ and $(b_C/b_W) = 0.4$. The flat fuselage provides the possibility of systematically varying the canard position and attitude relative to the wing. Three-component (lift, drag, and pitching moment), surface-pressure, and flowfield measurements using a conventional five-hole probe, as well as flow visualizations by means of oil-flow patterns, have been performed in the Institute's 1.3-m low-speed wind tunnel. Additional flow visualizations in a small water tunnel have also been carried out. The investigations were concerned with the wing-alone and canard-wing combination in order to detect interference effects. The achieved results of this survey have already been partly published in Refs. 33-35. Further results of flowfield measurements, which show the development of the canard wake over the wing in detail, are being presented here. Another canard configuration under consideration is the configuration of the International Vortex Flow Experiment on Euler-Code Validation. The investigations on this configuration are documented in Ref. 36; they are not discussed here.

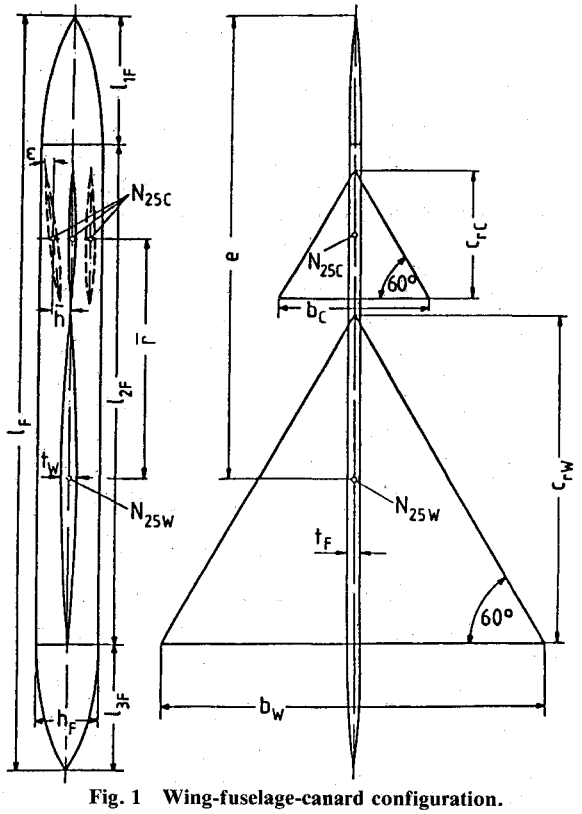

Fig. 1 Wing-fuselage-canard configuration.

Experimental Setup and Test Program

Models

The investigated wing-fuselage-canard configurations is shown in Fig. 1. The geometric data may be taken from Table 1.

The wing and canard have delta planforms of aspect ratio $A_C = A_W = 2.31$ and a corresponding leading-edge sweep of $\phi_C = \phi_W = 60$ deg. In both cases, symmetric parabolic arc airfoils for the root section and parabolic contours in spanwise direction have been used. The leading edges are sharp. Both

Table 1 Geometric data of the configuration

Canard:	Aspect ratio	$A_C = 2.31$
	Leading-edge sweep	$\phi_C = 60$ deg
	Thickness ratio	$(t/c_r)_C = 0.05$
Wing:	Aspect ratio	$A_W = 2.31$
	Leading-edge sweep	$\phi_W = 60$ deg
	Thickness ratio	$(t/c_r)_W = 0.05$
Fuselage:	Height ratio	$(h/l)_F = 1/12$
	Thickness ratio	$(t/l)_F = 1/60$
Combination wing-fuselage:		
	Relative fuselage length	$l_F/b_W = 2.0$
	Relative fuselage width	$t_F/b_W = 1/30$
	Rear position of N_{25W}	$e/l_F = 0.617$
Combination canard-wing:		
	Relative canard size	$b_C/b_W = 0.4$ $S_C/S_W = 0.16$
	Vertical position	$-0.04 \leq H \leq 0.04$
	Horizontal position	$-0.08 \leq R \leq 0.16$
	Setting angle	-12 deg $\leq \epsilon \leq 12$ deg

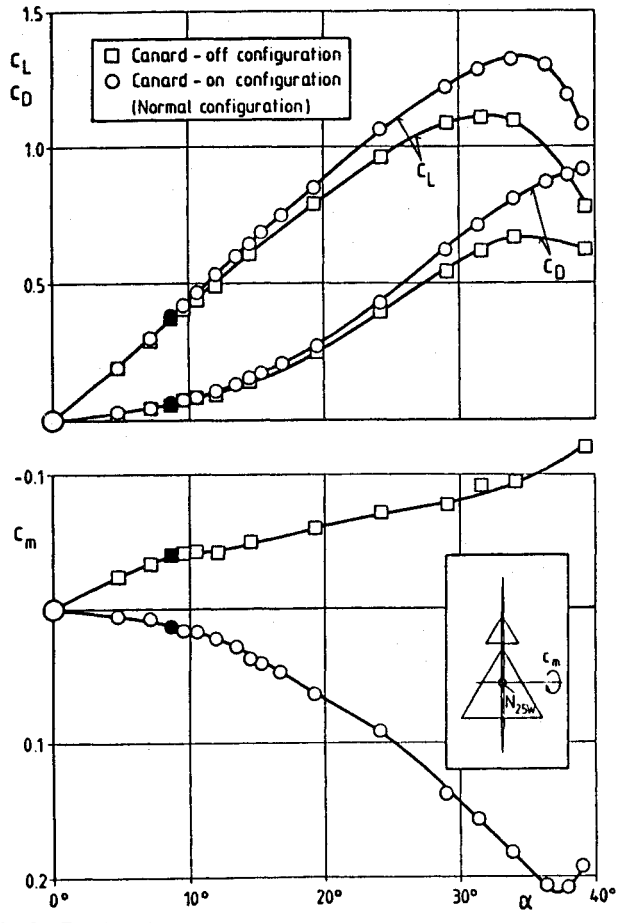

Fig. 2 Results of three-component measurements for the canard-off and canard-on normal configuration at $Re = 10^6$.

wing and canard are equipped with a tube system underneath the surface and pressure holes in order to measure the surface-pressure distribution. A very flat fuselage has been chosen to keep the canard in position relative to the wing, to provide some variation of this position, and to cover some volume necessary for the rubber tubes in the case of pressure distribution measurements. The fuselage consists of a cylindrical portion of length $l_{2F} = 8h_F$, and attached are front and rear parts of length $l_{1F} = l_{3F} = 2h_F$. Their shape has been taken as a polynomial of fourth order that meets the cylindrical part continuously with respect to slope and curvature. The wind-tunnel model was produced with $b_W = 600$ mm.

The wing was added to the fuselage in such a way that the trailing edge coincided with the rear end of the cylindrical part of the fuselage. Concerning the canard-wing combination, some variations in vertical and horizontal position and in setting angle of the canard were possible. The corresponding ranges may be taken from Table 1. A typical configuration has been chosen as a basis for comparisons. Its parameters are

$$\epsilon = 0 \text{ deg}, \qquad H = 0, \qquad R = 0.05$$

and it is called, subsequently, the "normal configuration."

Description of the Tests

The wind-tunnel investigations have been carried out at freestream velocities of $V_\infty = 30$ and 40 m/s, which correspond to Reynolds numbers of 10^6 and 1.4×10^6.

Three-component measurements (lift, drag, and pitching moment) have been performed for $-5 \text{ deg} \le \alpha \le 40$ deg, with $\Delta\alpha = 2.5$ deg. The surface-pressure measurements have been carried out on the suction side for seven selected angles of attack only. The flow on the upper surface of the configuration has been studied by means of oil-flow patterns. For this

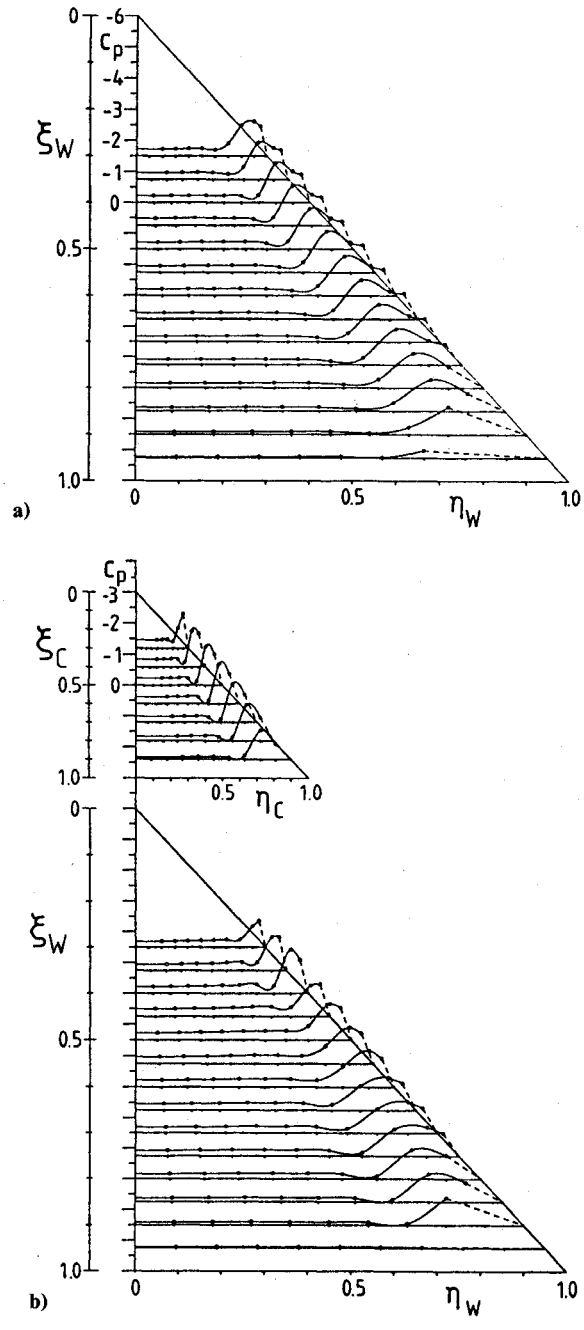

Fig. 3 Upper surface-pressure distribution at $\alpha = 8.7$ deg and $Re = 1.4 \times 10^6$: a) canard-off configuration, and b) canard-on normal configuration.

purpose, the black model surface was painted by a mixture of aluminum-oxide powder (1g), petroleum ($3cm^3$), and benzine ($1cm^3$), and exposed to the flow for about 30 s. The investigations mentioned thus far were made for the normal configuration and for a large variety of other canard positions. In order to get data for a comparison with the noninterfering case, investigations were extended to the wing-fuselage configuration without the canard.

Flowfield measurements were carried out in planes perpendicular to the freestream using a conical five-hole probe of 2 mm diam; the probe hole diameter is 0.3 mm. These measurements were performed with the normal configuration at stations $\xi_W = 0$, 0.3, 0.6, and 0.8 over the wing and at stations $\xi_W = 1.01$ and 1.125 downstream of the wing. In order to detect interference effects, the flowfield measurements were extended to the wing-fuselage configuration without canard at stations $\xi_W = 0.3$, 0.6, and 0.8 over the wing and at station

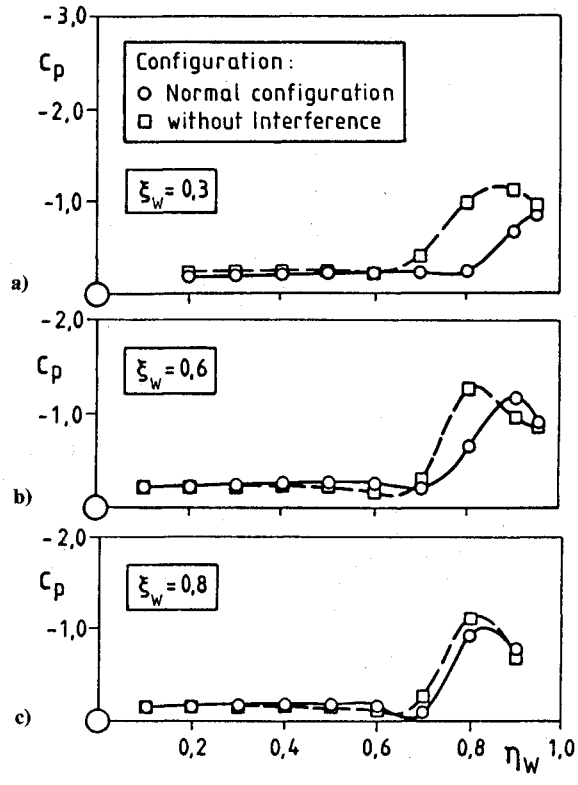

Fig. 4 Direct comparison of the upper surface-pressure distributions between the canard-off and the canard-on normal configuration at $Re = 1.4 \times 10^6$.

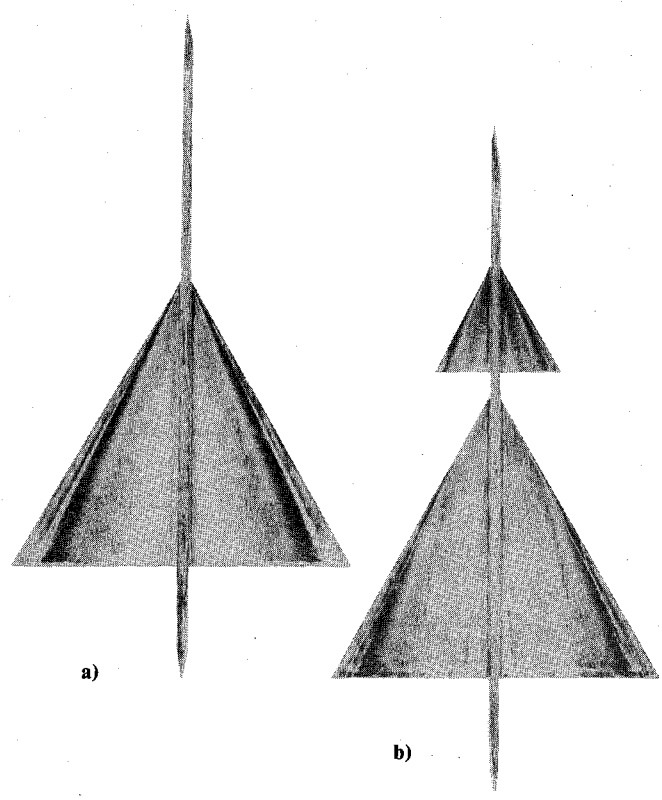

Fig. 5 Upper-surface oil-flow pattern at $\alpha = 8.7$ deg and $Re = 1.4 \times 10^6$: a) canard-off configuration, and b) canard-on normal configuration.

$\xi_W = 1.01$ downstream of the wing. In all cases, the angle of attack was $\alpha = 8.7$ deg, where vortex breakdown is present neither for the wing-fuselage configuration nor for the canard-on normal configuration.

Results

Major interference effects between canard and wing have been studied by means of the canard-on normal configuration and the canard-off configuration. The results of these investigations have been published in Refs. 33 and 34. The main outcome is to be repeated here, since the knowledge of these results is essential for the understanding of the flowfield measurements presented in this paper.

The results of the three-component measurements for the canard-off and the canard-on normal configuration are presented in Fig. 2. For low angles of attack, both configurations have nearly the same lift and drag. The addition of the canard to the wing-fuselage configuration changes a formerly nose-down pitching moment to a nose-up pitching moment. The results of the corresponding surface-pressure measurements at $\alpha = 8.7$ deg, marked in Fig. 2 by the black symbols, are presented in Fig. 3. The traces of the leading-edge vortices can be detected from the suction peaks on both configurations, and it can clearly be seen that vortex breakdown does not take place at this angle of attack. A comparison between Figs. 3a and 3b reveals two characteristics of the flow around the canard configuration. The pressure distribution on the canard is very similar to the one on the wing alone, and in both cases the flow is fairly conical, apart from the trailing-edge region. On the wing of the canard configuration, the pressure distribution shows considerably lower suction peaks in the front part, which also lie closer to the leading edge than in the noninterfering case. This can be seen more easily in Fig. 4 in a direct comparison of pressure distributions on the wing for the canard configuration and the noninterfering case. This comparison is taken at the same measuring stations, where the flowfield measurements presented in this paper have been performed. Figure 4a shows at $\xi_W = 0.3$ for the canard-off configuration a suction peak, which results from a developed vortex. On the contrary, it shows for the canard configuration a suction peak that is smaller and lies very close to the leading edge. This "little" suction peak can only, if at all, result from a small vortex. At $\xi_W = 0.6$, Fig. 4b shows for both cases suction peaks resulting from developed vortices. For the canard configuration, the suction peak lies closer to the leading edge than for the noninterfering case. At $\xi_W = 0.8$, (Fig. 4c) the suction peak on the canard configuration has finally almost reached the size and position of the suction peak on the wing of the canard-off configuration. Figure 4 shows that the flow on the wing of the canard configuration is distinctly nonconical. This review ends with the presentation of the flow visualization by surface oil-flow patterns at $\alpha = 8.7$ deg. Figure 5a shows the result for the noninterfering case, and one can detect the traces of vortices with the aid of primary attachment and secondary separation lines. The flow is fairly conical. Figure 5b shows a very similar pattern on the canard of the canard configuration. The streamlines on the wing of this configuration, however, are distinctly different from the noninterfering case. Primary attachment and secondary separation lines indicate that the wing vortices start a fair distance downstream of the wing apex. On the inner portion of the leading edge either an attached flow or a very weak flow separation is present. This delay in the formation of leading-edge vortices coincides with the smaller suction peaks of the pressure distributions, which were presented in Figs. 3 and 4a. It can also clearly be seen that the flow on the wing of the canard configuration is highly nonconical. Figure 5 shows, again, that vortex breakdown is not present at this angle of attack.

The presentation of these results reveals that there is a strong influence of the canard on the wing at this small angle of attack: the canard induces behind its trailing edge a downwash field within its span and an upwash field outside its span. The downwash field reduces the effective angle of attack in the forward and inner portion of the wing considerably. This leads to a suppression of flow separation there. The upwash field increases the effective angle of attack in the outside and rear

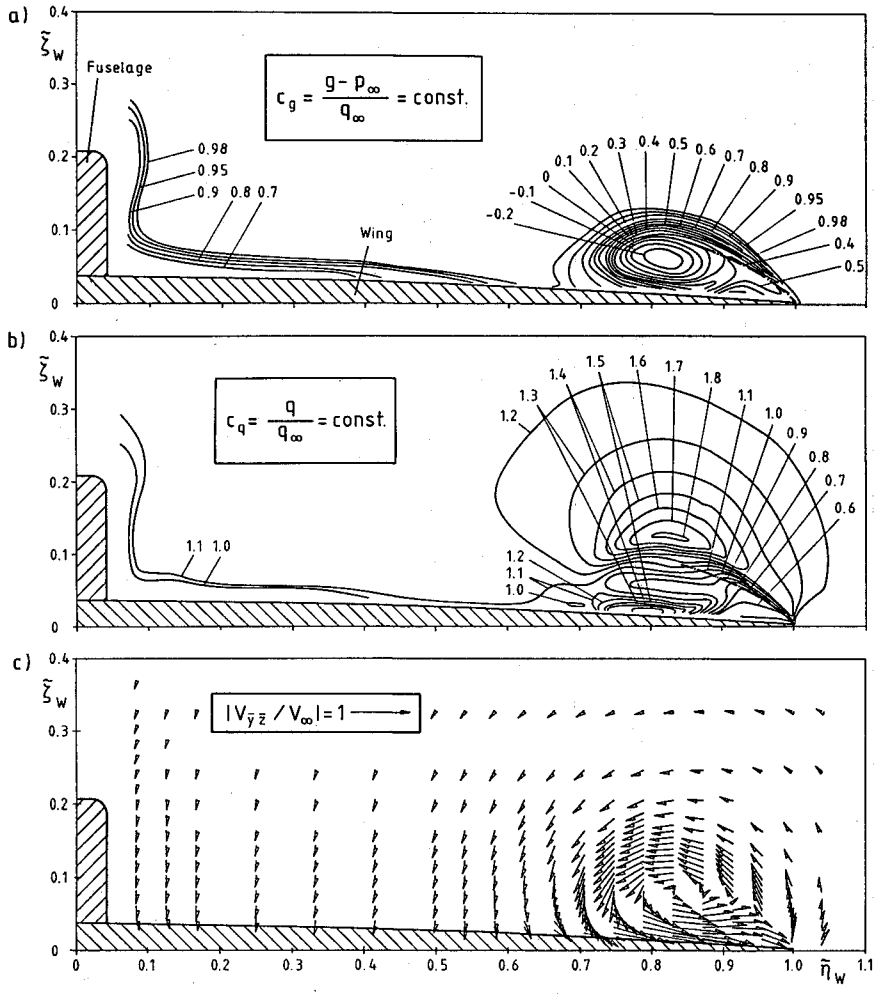

Fig. 6 Results of flowfield measurements over the canard-off configuration at $\xi_W = 0.8$, $\alpha = 8.7$ deg, and $Re = 1.4 \times 10^6$: a) total pressure isobars, b) dynamic pressure isobars, and c) projection of the velocity vector into the measuring plane.

portion of the wing, which supports flow separation there. This mechanism leads to a delayed formation of the wing vortex downstream of the wing apex. Because of the nonuniform distribution of the effective angle of attack along the leading edge of the wing, the wing vortex is fed with vorticity in a different manner than it is known from the noninterfering case. For this reason, it is possible that the suction peak in the surface pressure distribution of the wing vortex at $\xi_W = 0.8$ (see Fig. 4c) almost reaches the size and location of the suction peak, which is induced by the vortex in the noninterfering case. In total, however, the wing works at a lower angle of attack than in the noninterfering case, which leads to a compensation of the additional lift at the canard through a loss of lift at the wing. Therefore, both configurations have almost the same lift. At $\alpha = 8.7$ deg, the influence of the wing on the canard is very small. These mechanisms of mutual interference have already been described—at least partly—by other authors (see e.g., Behrbohm[1]).

All investigations performed so far have not revealed how the vortices coming from the canard behave over the wing of the configuration. No information could be obtained on the location and the structure of the canard wake in this region of the flowfield. In order to clarify this situation, extensive flowfield measurements have been carried out for the canard-on normal configuration and the canard-off configuration. The investigation of both cases yields the possibility of comparison between corresponding results, and so interference effects can be detected easily. Because a conventional five-hole proble was used, these measurements were limited to flowfields without vortex breakdown. The angle of attack was, therefore, chosen at $\alpha = 8.7$ deg.

Documentation of the Three-Dimensional Flowfield for the Canard-off Configuration

The documentation of the three-dimensional flowfield for the canard-off configuration was carried out at several planes $\xi_W = \text{const}$. The obtained results are very similar, which is due to the "conicality" of the flow (see Figs. 3a and 5a). Therefore, only results of the measurements for one plane $\xi_W = \text{const}$ will be presented here.

Figure 6 shows the results that were obtained in the measuring plane $\xi_W = 0.8$. It presents lines of constant total pressure c_g (see Fig. 6a), lines of constant dynamic pressure c_q (see Fig. 6b), and the velocity vector component in the measuring plane (see Fig. 6c). The isobars of total pressure in Fig. 6a clearly indicate those regions of the flowfield where energy losses are present. Above the center part of the wing and the fuselage these losses emanate from the corresponding boundary layers. Local flow separation may be present in the region of the wing-fuselage junction and also on the fuselage, but these phenomena are too small and too close to the wall in order to be detected with the five-hole probe used in this investigation. The large total pressure-loss region in the right-hand part of the figure is due to the leading-edge vortex system. The center of the primary vortex is found at the location of minimum total pressure, which is at $\tilde{\eta}_W = 0.82$ and $\tilde{\zeta}_W = 0.06$. This vortex is accompanied by a secondary vortex, which is due to secondary flow separation below the primary vortex. The center of the secondary vortex lies at approximately $\tilde{\eta}_W = 0.93$ and $\tilde{\zeta}_W = 0.02$. The secondary vortex is rather small because the boundary layer on the wing beneath the primary vortex is turbulent. For this reason, secondary flow separation occurs rather close to the leading edge, which leads to a small sec-

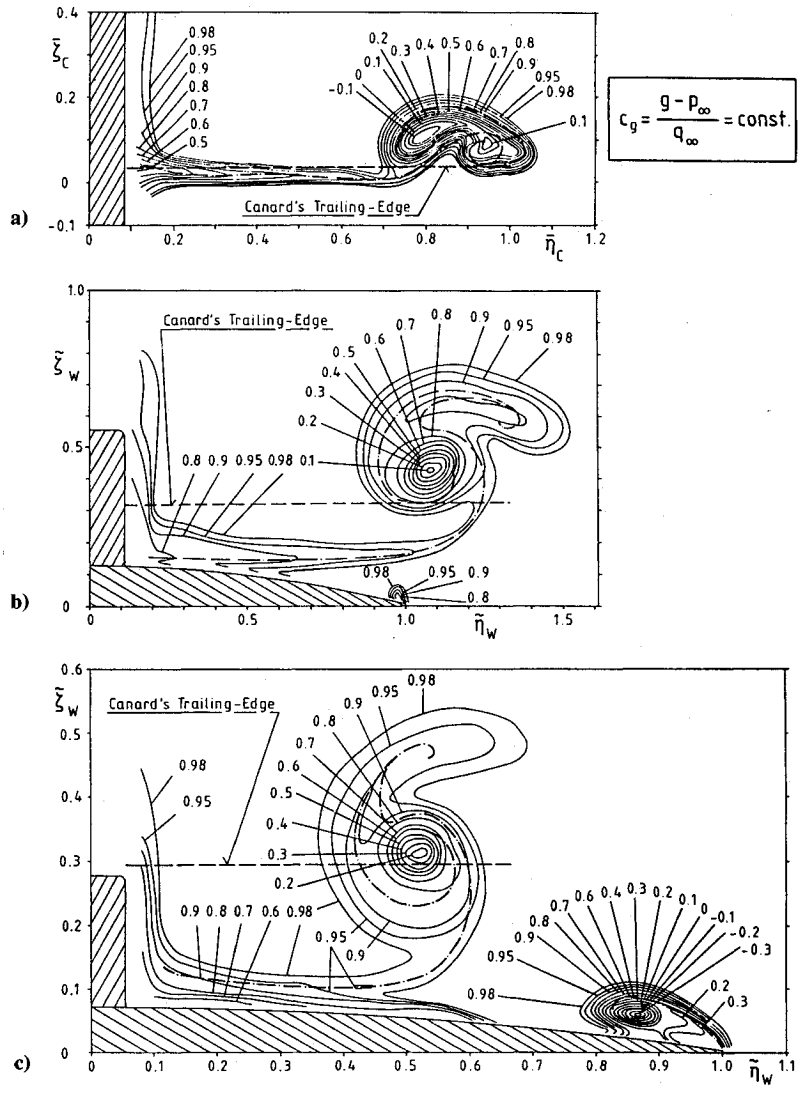

Fig. 7 Results of flowfield measurements over the canard-on normal configuration at $\alpha = 8.7$ deg, and $Re = 1.4 \times 10^6$. Total pressure isobars at a) $\xi_W = 0$, b) $\xi_W = 0.3$, and c) $\xi_W = 0.6$.

ondary vortex. This effect has been investigated for delta wings by Hummel.[37] The location of the vorticity sheet coming from the leading edge is indicated by a dash-dotted line. It was found by searching for relative minimum values in the total pressure distribution.

Figure 6b shows the isobars of dynamic pressure, and Fig. 6c presents the projection of the corresponding velocity vector into the measuring plane. The boundary layers on the wing and the fuselage are clearly indicated by losses of dynamic pressure. The center of the primary vortex at $\tilde{\eta}_W = 0.82$ and $\tilde{\zeta}_W = 0.06$ lies in a region with a relative minimum of dynamic pressure. Also, the secondary vortex is indicated by a region with low dynamic pressure. Below the center of the primary vortex an increase of dynamic pressure is present, which leads to a relative maximum there. A second relative maximum appears above the center of the primary vortex just outside of the region, where total pressure losses are present (see Figs. 6a and 6b). From this presentation, it is obvious that at the test Reynolds number of 1.4×10^6 the velocity distribution within the wing vortex system is strongly influenced by viscous effects in a rather large area around the center of the primary vortex. The increase of velocity on a line from above the primary vortex through its center is stopped at the border, where total pressure losses start to dominate the flow. Beginning there, the velocity vector decreases as the center of the vortex is approached (see Fig. 6c). This type of velocity field is well known for trailing vortices behind wings with attached flow, which are mainly under the influence of viscous decay as described by Oseen,[38] Newman,[39] and Dosanjh et al.,[40] for example. The shape of the velocity field within the leading-edge vortex of this wing here is very different from the velocity field of a potential vortex. The results given in this section can now be used for comparisons with the measurements above the canard configuration, which will be presented in the following section.

Documentation of the Three-Dimensional Flowfield for the Canard-on Configuration

The documentation of the three-dimensional flowfield for the canard-on normal configuration is performed with the presentation of total pressure isobars for each measuring plane. The results of the investigations above the forward part of the wing of the normal configuration are given in Fig. 7. The first measuring plane is located at the apex of the wing at $\xi_W = 0$, which is equal to $\xi_C = 1.125$. The result is shown in Fig. 7a: regions of total pressure loss indicate the fuselage's boundary layer and the inner portion of the canard's trailing-edge wake, which is a vorticity sheet. In the region of $0.7 \leq \bar{\eta}_C \leq 1.1$, a relatively large area of total pressure losses represents the vortex system of the canard. This vortex system consists of the canard's primary vortex with its center at $\bar{\eta}_C = 0.8$ and of the already fully developed trailing-edge vortex at $\bar{\eta}_C = 0.93$. At this measuring station, the secondary vortex can hardly be detected, because it has no longer been fed with vorticity since it left the canard's trailing edge. Both vortices, however, are counter-rotating with respect to the primary vortex. A detailed survey on the development of a delta wing's trailing-edge vortex and the behavior of the secondary vortex is given by Hummel.[37] The results, according to Refs. 33 and 34, have revealed that there exists almost no influence of the wing on the canard at this angle of attack, $\alpha = 8.7$ deg. Therefore, the result of Fig. 7a also can be considered as a documen-

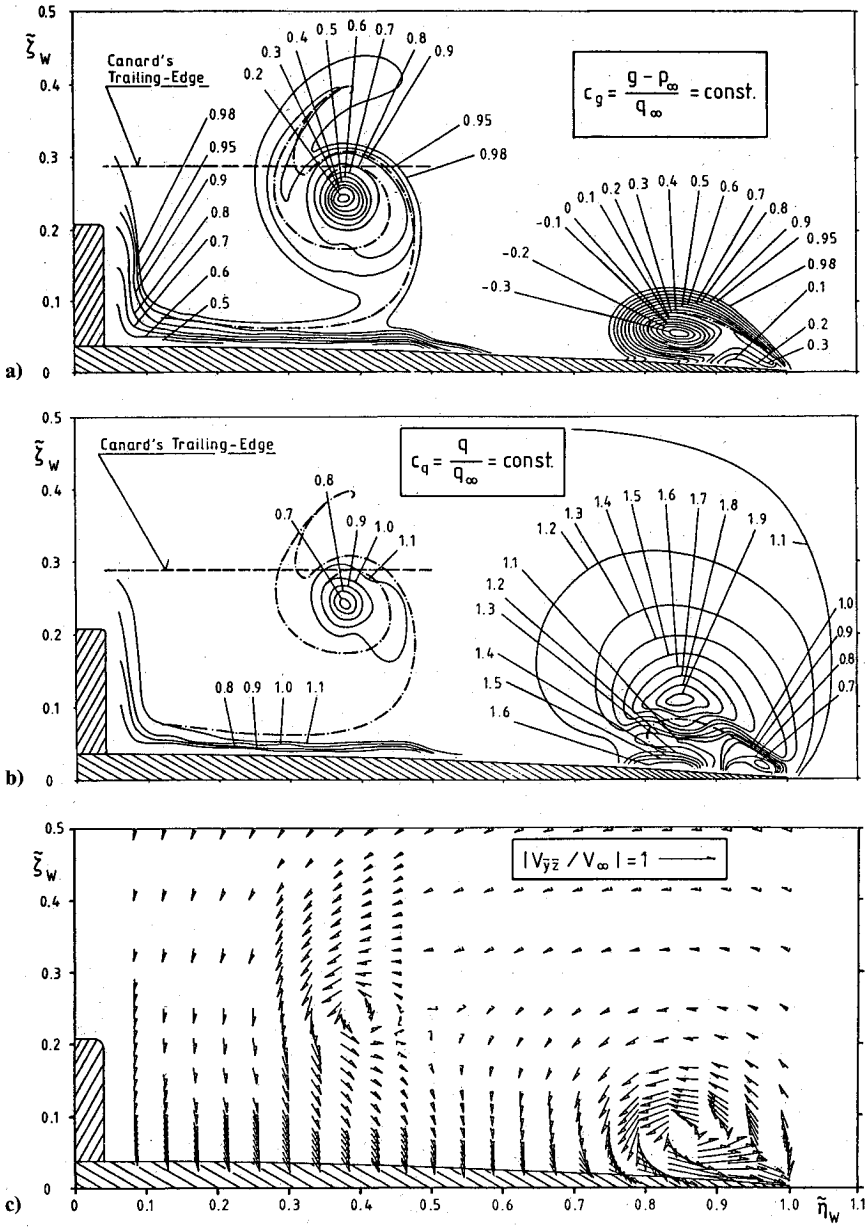

Fig. 8 Results of flowfield measurements over the canard-on normal configuration at $\xi_W = 0.8$, $\alpha = 8.7$ deg, and $Re = 1.4 \times 10^6$: a) total pressure isobars, b) dynamic pressure isobars, and c) projection of the velocity vector into the measuring plane.

tation of the flow behind a delta wing without interference.

The results of the second measuring plane at $\xi_W = 0.3$ are given in Fig. 7b. Again, total pressure losses indicate where the boundary layer of the fuselage is located. Detailed investigations of the flow above the fuselage were not performed. The vorticity sheet coming from the trailing edge of the canard has "touched" the upper surface of the wing for $\tilde{\eta}_W \leq 0.6$. Therefore, in this region a fusion of the canard's vorticity sheet with the suction-side boundary layer of the wing has taken place. For $\tilde{\eta}_W \geq 0.6$, the vorticity sheet has again separated from the wing, and it rolls into the canard's vortex system. The center of the primary vortex of the canard can be detected at $\tilde{\eta}_W = 1.1$ and $\tilde{\zeta}_W = 0.4$ by the absolute minimum of total pressure. The trailing-edge vortex has turned around the primary vortex in the sense of rotation of the primary vortex. During this process the corresponding total pressure losses are spread out, and their intensity is weakened considerably. At this measuring station only a very small primary vortex is present at the wing. This is due to the strong canard-induced downwash at the wing leading edge (see Fig. 4a).

The results of the third measuring plane at $\xi_W = 0.6$ are given in Fig. 7c. The process of fusion between the vorticity sheet from the canard and the suction-side boundary layer of the wing has advanced. This leads to a rather thick layer of total pressure losses on the suction side of the wing. The vorticity sheet separates again from the wing at approximately $\tilde{\eta}_W = 0.45$ and rolls into the vortex system of the canard, which lies with the center of its primary vortex at $\tilde{\eta}_W = 0.5$ and $\tilde{\zeta}_W = 0.31$. The total pressure losses associated with the trailing-edge vortex have rotated further around the primary vortex in the sense of rotation of the primary vortex. The level of these pressure losses has also further decreased. At this station the canard vortex system is completely within the local wing span, and the induced velocities of this sytem at the leading edge of the wing are, therefore, directed upwards. This situation favors flow separation at the wing leading edge, and a relatively large area of total pressure losses associated with a wing vortex system can be found above the wing. The center of the primary vortex lies at $\tilde{\eta}_W = 0.87$ and $\tilde{\zeta}_W = 0.06$, whereas the center of the corresponding secondary vortex lies at $\tilde{\eta}_W = 0.95$ very close to the wing surface. The small secondary vortex indicates that the flow beneath the primary vortex is turbulent. The relative size of the wing vortex system is considerably smaller than in the noninterfering case, as it is revealed in a comparison with Fig. 6a, which is valid since the flow over the wing without canard is fairly conical.

Figure 8 presents the results of the flowfield measurements for the fourth station at $\xi_W = 0.8$; they are presented in the same manner as shown for the noninterfering case at the same measuring station in Fig. 6. Figure 8a shows the isobars of

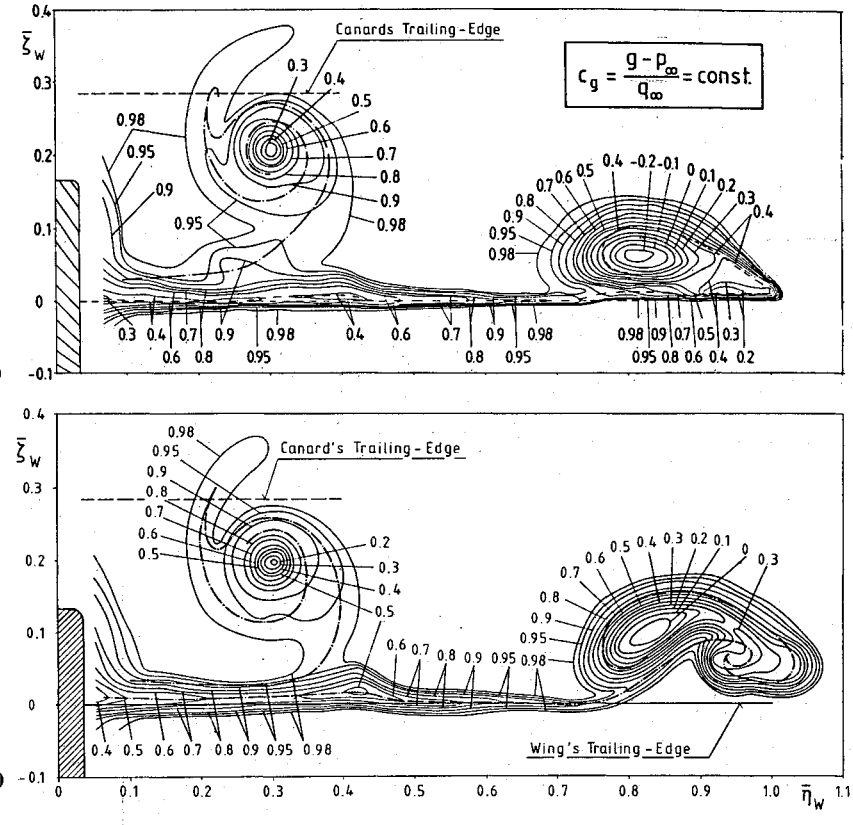

Fig. 9 Results of flowfield measurements behind the canard-on normal configuration at $\alpha = 8.7$ deg, and $Re = 1.4 \times 10^6$. Total pressure isobars at a) $\xi_W = 1.01$, and b) $\xi_W = 1.125$.

total pressure. Compared with the results of the upstream station at $\xi_W = 0.6$ (see Fig. 7c), no principal differences can be found. Only the relative size of the wing vortex at $\xi_W = 0.8$ has grown slightly, but it has not yet reached the relative size of the wing vortex in the noninterfering case, which is revealed through a comparison between Figs. 6a and 8a. Figure 8b shows the isobars of dynamic pressure. The wing vortex is dominated by strong viscous effects in the same manner as it was found for the noninterfering case (see Fig. 6b). At the location of the canard vortex system, a relatively flat distribution of dynamic pressure with small gradients can be found. The projection of the local velocity vector into the measuring plane in Fig. 8c shows a distinctly rotating velocity field, which still indicates the location of the canard vortex over the wing. The presentation of the results from above the wing of the normal configuration shows that the canard vortex system is moved inwards and downwards toward the wing surface as it passes downstream.

Figure 9 presents the results of the flowfield measurements behind the wing. The situation just downstream of the trailing edge at $\xi_W = 1.01$ is given in Fig. 9a. The process of fusion between the vorticity sheet from the canard and the suction-side boundary layer of the wing has led to a rather thick wake coming from the trailing edge of the wing for $\bar{\eta}_W \leq 0.45$. The vorticity sheet of the canard separates from this wake and rolls into the canard vortex system as observed earlier. The total pressure losses of the canard vortex system still show regions that can be associated with the canard's trailing-edge vortex. The relative size of the wing vortex has grown again. A comparison with Fig. 6a reveals that the wing vortex has now reached the same relative size as the wing vortex of the noninterfering case. The canard-induced upwash along the wing leading edge causes an increase of effective angle of attack there that in turn supports flow separation at the leading edge. This mechanism is responsible for the growth of the wing vortex along the leading edge from the almost negligibly small size at $\xi_W = 0.3$ (see Fig. 7b) up to the same relative size of the vortex of the noninterfering case, which is reached at the trailing edge of the wing (see Figs. 6a and 9a). This also means that the wing vortex of the canard configuration is fed with vorticity in a different manner along the leading edge than in the noninterfering case. The presentation of the preceding figures also indicates that the flow over the canard configuration is highly nonconical.

The results of the measurements in the last plane at $\xi_W = 1.125$ are presented in Fig. 9b. Concerning the canard vortex system, principal changes have not occurred. The wing primary vortex is now accompanied by a distinct counter-rotating, trailing-edge vortex. At $\bar{\eta}_W = 0.42$, one can detect a small relative minimum of total pressure in the wake coming from the wing trailing edge that results from the separation process between the vorticity sheet from the canard and the suction-side boundary layer of the wing. This relative minimum may represent the total pressure losses of a small vortex, which lies inside the trailing-edge wake. This vortex may also be present above the wing at $\bar{\eta}_W = 0.47$, (see Fig. 8a). The corresponding oil-flow pattern supports this idea (see Fig. 5b): in the vicinity of the trailing edge at approximately $\eta_W = 0.42$, a slight convergence of the wall streamlines is observed, which might be an indication of small and local flow separation. Unfortunately, this phenomenon is too small in order to be resolved properly with the five-hole probe in use or even with the given surface-pressure distribution measurements, because the distance between two pressure tabs of $\Delta\eta_W = 0.1$ is relatively large.

Another outcome of the flowfield measurements is the distribution of the static pressure in each measuring plane. Because of limited space, these results will not be presented here. Only a conclusive overview is given in Fig. 10. This figure represents the distribution of minimum static pressure in each measuring plane as a function of the longitudinal coordinate ξ_W. Minimum static pressure always occurs in the center of the primary vortices. Figure 10 shows for the noninterfering case a constant value of minimum static pressure in the center of the primary vortex over the wing, which experiences a steep positive pressure gradient as the trailing edge is approached. This behavior again indicates that the flow around the canard-off configuration is fairly conical above the forward part of the wing. It is known from Refs. 33 and 34 that the flow over the canard is not significantly influenced by the wing at this

angle of attack. Therefore, the distribution of minimum static pressure for the noninterfering case is also used for the canard of the normal configuration (see Fig. 10). Through this method, one achieves the distribution of minimum static pressure in the center of the canard's primary vortex from above the canard up to positions downstream of the wing trailing edge. From the trailing edge of the canard to the apex of the wing, the minimum static pressure increases further. Over the wing, the value of minimum static pressure within the canard's primary vortex decreases, and toward the trailing edge of the wing the value of minimum static pressure increases again, but not as steep as in the vicinity of the canard's trailing edge. The decrease of minimum static pressure above the wing is caused by the wing flow. It is due to the lift, which is generated by the wing. This decrease of static pressure can be interpreted as an acceleration of the vortical flow coming from the canard. At larger angles of attack, when the canard vortices burst above the canard, this situation is responsible for the process of restoring the burst canard vortices back into a nonburst state. This phenomenon is documented in detail in Refs. 33 and 34. Finally, the distribution of minimum static pressure of the wing vortex of the normal configuration shows much lower values than for the noninterfering case. This again is an illustration of the nonuniform vorticity feeding mechanism of the wing vortex at the canard configuration.

At the end of this documentation, Fig. 11 gives a global overview of the three-dimensional flowfield above the canard-on normal configuration, as it is understood by the authors. For this presentation, the effects of viscosity have been neglected, wing and canard are considered to be flat plates, and no fuselage is taken into account. Figure 11 illustrates how the canard vortex system develops, and how this system is located above the wing. The shaded area, which lies in Fig. 11 toward the centerline of the configuration, shows that region of the wing, where the vorticity sheet of the canard joins the suction-side boundary layer of the wing, as documented in the preceding figures. This means for the simplified case of Fig. 11 that the free vorticity sheet coming from the canard joins the wing-fixed vorticity sheet. Therefore, in the shaded region of the wing, instead of two, only one combined vorticity sheet is present. Finally, behind the wing one can clearly see a system of four vortices on the right-hand side of the configuration. These vortices were generated during the course of the flow, and there is one primary vortex each for canard and wing, which is accompanied by a corresponding trailing-edge vortex after having left either canard's or wing's trailing edge. These vortices are already existing in nonviscous flow. Figure 11 demonstrates the complexity of the flow, and it gives a guideline for numerical simulators in the sense that it shows all those features of the flow that should be an outcome of an inviscid flow theory.

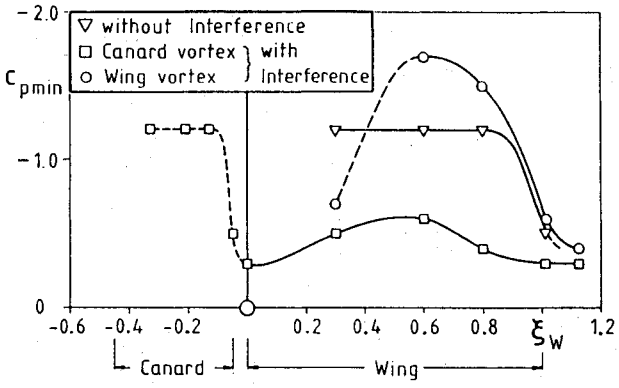

Fig. 10 Distribution of minimum static pressure in the center of the vortices of the canard-off and canard-on normal configuration at $\alpha = 8.7$ deg and $Re = 1.4 \times 10^6$.

Conclusions

Comprehensive aerodynamic investigations have been carried out on a close-coupled, $A = 2.31$, delta-canard configuration at low speed. Results of three-component, surface-pressure, and flowfield measurements as well as oil-flow patterns are presented for the canard-off and canard-on configurations. The flowfield measurements were carried out at $\alpha = 8.7$ deg, where vortex breakdown is not present over the configuration.

Major findings of these investigations are:

1) The vortices existing in both cases are strongly influenced by viscous effects at the test Reynolds number of 1.4×10^6. In regions with total pressure losses $c_g < 1$, a considerable decrease of flow velocity is present if the center of a vortex is approached. In a numerical simulation, this phenomenon will turn out by properly taking into account viscous effects.

2) The canard vortex system passes the wing leading edge relatively high above the configuration. Through wing influence, this system is moved above the wing inward toward the center of the configuration and also downward toward the wing surface. The canard vortex system consists of the canard's primary vortex and the corresponding trailing-edge vortex, which develops just downstream of the canard. This vortex system keeps its structure up to stations downstream of the wing trailing edge.

3) Because of induced velocities, the vorticity sheet coming from the canard's trailing edge is moved toward the upper wing surface, which leads to a fusion between this vorticity sheet and the suction-side boundary layer in the inner portion of the wing surface. In nonviscous flow, this process is equivalent to a fusion of the free canard vorticity sheet with the wing-bound vorticity sheet. Beneath the canard vortex the vorticity sheet of the canard separates from the wing surface again, and it rolls into the canard vortex system.

4) Because of the canard's downwash at the leading edge in the forward, inner portion of the wing, the effective angle of attack is reduced ther considerably. This leads to a suppression of flow separation, and the formation of the wing leading-edge

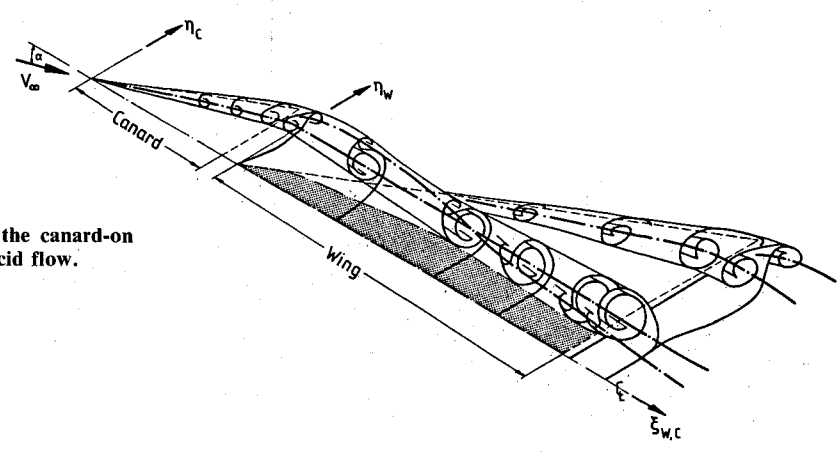

Fig. 11 Schematic overview of the flowfield above the canard-on normal configuration at low angle of attack and inviscid flow.

vortex is, therefore, delayed until the canard's induced upwash supports flow separation. Because of the nonuniform distribution of the effective angle of attack along the leading edge of the wing, the wing vortex is fed with vorticity in a different manner than it is known from the noninterfering case. Nevertheless, at the wing trailing edge the same relative size and position of the wing vortex is reached, as in the noninterfering case. The wing vortex system of the canard configuration is, therefore, highly nonconical.

Acknowledgment

These investigations have been supported by Deutsche Forschungs-gemeinschaft under Contract DFG Hu 254/8.

References

[1]Behrbohm, H., "Basic Low Speed Aerodynamics of the Short-Coupled Canard Configuration of Small Aspect Ratio," Saab, TN-60, Linköping, Sweden, July 1965.

[2]Bates, W. R., "Low-Speed Static Longitudinal Stability Characteristics of a Canard Model Having a 60° Triangular Wing and Horizontal Trail," NACA RM-L9H17, Nov. 1949.

[3]Bates, W. R., "Low-Speed Static Lateral Stability Characteristics of a Canard Model Having 60° Triangular Wing and Horizontal Tail," NACA RM-L9J12, Nov. 1949.

[4]Draper, J. W., "Low-Speed Static Stability Characteristics of a Canard Model with a 45° Sweptback Wing and a 60° Triangular Horizontal Control Surface," NACA RM-L50G11, Sept. 1950.

[5]Johnson, J. L., Jr., "A Study of the Flow Field Behind the Triangular Horizontal Tail of a Canard Airplane at Approximately the Vertical-Tail Location by Means of a Tuft Grid," NACA RM-L52H11, Oct. 1952.

[6]Burrows, D. L., "Large-Scale Low-Speed Wind-Tunnel Tests of a Model Having a 60° Delta Horizontal Canard Control Surface and Wing to Obtain Static-Longitudinal-Stability and Canard-Surface Hinge-Moment Data," NACA RM-L54D16a, June 1954.

[7]Sleeman, W. C., Jr., "Investigation at High Subsonic Speeds of the Static Longitudinal and Lateral Stability Characteristics of Two Canard Airplane Configurations," NACA RM-L 57J08, Dec. 1957.

[8]Scallion, W. I., "Low-Speed Longitudinal and Lateral Aerodynamic Characteristics of a Model with a Low-Aspect-Ratio Variable-Incidence Wing and with a Free-Floating and a Programed High-Lift Canard Control," NASA TN-D 1381, 1962.

[9]Lacey, D. W. and Chorney, St. C., "Subsonic Aerodynamic Characteristics of Close-Coupled Canards with Varying Area and Position Relative to a 50° Swept Wing," Naval Ship Research and Development Center, TN-AL-199, March 1971.

[10]Krouse, J. R., "Effects of Canard Planform on the Subsonic Aerodynamic Characteristics of a 25° and a 50° Swept-Wing Research Aircraft Model," Naval Ship Research and Development Center, Evaluation Rept. AL-91, May 1972.

[11]Ottensoser, J., "Wind Tunnel Data on the Transonic Aerodynamic Characteristics of Close Coupled Canards With Varying Planform Position and Deflection Relative to a 50° Swept Wing," Naval Ship Research and Development Center, Test Rept. AL-88, May 1972.

[12]Lacey, D. W., "Transonic Characteristics of Close-Coupled Canard and Horizontal Tail Installed on a 50 Degree Sweep Research Aircraft Model," Naval Ship Research and Development Center, Evaluation Rept. AL-81, Aug. 1972.

[13]Gloss, B. B. and McKinney, L. W., "Canard-Wing Lift Interference Related to Maneuvering Aircraft at Subsonic Speeds," NASA TM-X-2897, 1973.

[14]Gloss, B. B., "Effect of Canard Location and Size on Canard-Wing Interference and Aerodynamic-Center Shift Related to Maneuvering Aircraft at Transonic Speeds," NASA TN-D-7505, June 1974.

[15]Henderson, W. P., "The Effect of Canard and Vertical Tails on the Aerodynamic Characteristics of a Model With a 59° Sweptback Wing at a Mach Number of 0.30," NASA TM-X-3088, Sept. 1974.

[16]Gloss, B. B., "The Effect of Canard Leading-Edge Sweep and Dihedral Angle on the Longitudinal and Lateral Aerodynamic Characteristics of a Close-Coupled Canard-Wing Configuration," NASA TN-D-7814, Dec. 1974.

[17]Gloss, B. B., "Effect of Wing Planform and Canard Location and Geometry on the Longitudinal Aerodynamic Characteristics of a Close-Coupled Canard Wing Model at Subsonic Speeds," NASA TN-D-7910, June 1975.

[18]Boyden, R. P., "Subsonic Dynamic Stability Characteristics of Two Close-Coupled Canard-Wing Configurations," NASA TP-1291, 1978.

[19]Gloss, B. B., "Effect of Camber on the Trimmed Lift Capability of a Close-Coupled Canard-Wing Configuration," NASA TM-78686, 1978.

[20]Gloss, B. B., Ray, E. J., and Washburn, K. E., "Effect of Canard Vertical Location, Size and Deflection on Canard-Wing Interference at Subsonic Speeds," NASA TM-78790, 1978.

[21]Eberle, R. B., Stancil, R. T., and Fowler, W. C., "A Critical Review of Canard Relative to Aft Horizontal Tail Based on Low- and High-Speed Tunnel Tests of a Fighter/Attack Configuration," AIAA Paper 71-8, Jan. 1971.

[22]Goldstein, S. E. and Combs, C. P., "Trimmed Drag and Maximum Flight Efficiency of Aft Tail and Canard Configurations," AIAA Paper 74-69, Feb. 1974.

[23]John, H. and Kraus, W., "High Angle of Attack Characteristics of Different Fighter Configurations," AGARD CP-247, 1978, pp. 2-1-2-12.

[24]Kraus, W., "Delta Canard Configuration at High Angle of Attack," *Zeitschrift für Flugwissewschaften und Weltram forschung,* Vol. 7, 1983, pp. 41–46.

[25]Gloss, B. B. and Miner, D. D., "Flow Visualization Study of Close-Coupled Canard-Wing and Strake-Wing Configurations," NASA TM-X-75663, 1975.

[26]Lorincz, D. J., "Flow Visualization Study of the HIMAT RPRV," NASA CP-163094, 1980.

[27]Er-El, J. and Seginer, A., "Vortex Trajectories and Breakdown on Wing-Canard Configurations," *Journal of Aircraft,* Vol. 22, Aug. 1985, pp. 641–648.

[28]Gallington, R. and Sisson, G., "Flow Visualization Using a Computerized Data Aquisition System," *Preprints of the Contributed Papers, International Symposium on Flow Visualization, Ruhr Universität Bochum,* Institut für Thermo-und Fluiddynamik, Bachum, 1980, pp. 134–141.

[29]Griffin, K. E., "Measurement of Wake Interactions of a Canard and a Forward Swept Wing," U.S. Air Force Academy, Colorado Springs, CO, USAFA, TN-82-4, July 1982.

[30]Griffin, K. E., Haerter, E. C., and Smith, B. R., "Wake Characteristics and Interactions of the Canard/Wing Lifting Surface Configuration of the X-29 Forward Swept Wing Flight Demonstrator," U.S. Air Force Academy, Colorado Springs, CO, USAFA TN-83-7, Aug. 1983.

[31]Griffin, K. E. and Jonas, F. M., "Wake Characteristics and Interactions of the Canard Wing Lifting Surface Configuration of the X-29 Forward Swept Wing Flight Demonstrator," AIAA Paper 83-1835, 1983.

[32]Hjelmberg, K., "Test on a 55° and 65° Delta Wing at FFA," *Symposium on International Vortex Flow Experiment on Euler Code Validation, Stockholm,* Flygtekniska Forsöksanstalten, Bromma, Sweden, 1986, pp. 89–106.

[33]Hummel, D. and Oelker, H., "Vortex Interference Effects on Close-Coupled Canard Configurations in Incompressible Flow," *Symposium on International Vortex Flow Experiment on Euler Code Validation, Stockholm,* Flygtekniska Forsöksanstalten, Bromma, Sweden, 1986, pp. 47–61.

[34]Oelker, H. and Hummel, D., "Experimentelle Untersuchungen an Entenkonfigurationen," DGLR-Bericht 86-03, DGLR 1986, pp. 172–191.

[35]Hummel, D., "Documentation of Separated Flows for Computational Fluid Dynamics Validation," AGARD CP-437, 1988, pp. Vol. 2, pp. PIS-1-PIS-24.

[36]Oelker, H., "Aerodynamische Untersuchungen an kurzgekoppelten Entenkonfigurationen," Ph.D. Dissertation, Technical University of Braunschweig, Braunschweig, 1989.

[37]Hummel, D., "On the Vortex Formation Over a Slender Wing at Large Angles of Incidence," AGARD CP-247, 1978, pp. 15-1–15-17.

[38]Oseen, C. W., "Über Wirbelbewegung in einer reibenden Flüssigkeit," *Arkiv för Mathematik, Astronomic och Fysik,* Vol. 7, No. 14, 1911, pp. 1–13.

[39]Newman, B. G., "Flow in a Viscous Trailing Vortex," *Aeronautical Quarterly,* Vol. 10, May 1959, pp. 149–162.

[40]Dosanjh, D. S., Gasparek, E. P., and Eskinazi, S., "Decay of a Viscous Trailing Vortex," *Aeronautical Quarterly,* Vol. 13, May 1962, pp. 167–188.